Chapter 2
Nature and Variability of Plasmas Ejected by the Sun

J.-C. Vial

Abstract The Sun not only emits radiation in the whole electromagnetic spectrum but also sends in the interplanetary medium plasmas of different natures (energy, continuous, or episodic flows, etc.) which contribute to its (small) mass loss. The escaping material when properly oriented may impact on the Earth magnetic environment with cascading effects on the Earth atmosphere. The continuous flow known as the solar wind is actually made of two categories, slow and fast winds. We discuss their properties, sources, and the mechanisms at work through the two types of models (fluid and particles). We describe the sporadic mass losses for the three main typical events: flares, prominence ejection, and coronal mass ejection. We discuss a possible unifying scenario which takes into account these three manifestations of magnetic disruption. We also extend the investigation to the whole heliosphere. Our conclusion proposes a few goals concerning the diagnostic and the understanding of the plasmas ejected by the Sun, along with the space missions which could provide some answers.

2.1 Introduction

We first recall some properties of the Sun from its internal structure to the outer heliosphere. We provide some basic parameters of the outer atmosphere which allow us to define a quiet Sun coronal model. In the second part, we derive that the corona cannot be in hydrostatic equilibrium and that necessarily a wind blows. In the third part, we establish the Sun permanent loss rate and characterize the two kinds of solar wind. We also raise the (open) issue of the "sources" of the fast and slow winds. In the fourth part, we compare the pros and cons of the fluid models with the kinetic/exospheric models. In the fifth part, we treat the activity-related solar plasma losses, an issue with has a strong impact on Space Weather. We show how flares, eruptive prominences (EPs), and Coronal Mass Ejections (CMEs) are closely related phenomena whose extension concerns the whole heliosphere, which

J.-C. Vial (✉)

Institut d'Astrophysique Spatiale, CNRS/Université Paris XI, Bâtiment 121, 91405 Orsay Cédex, France
e-mail: jean-claude.vial@ias.u-psud.fr
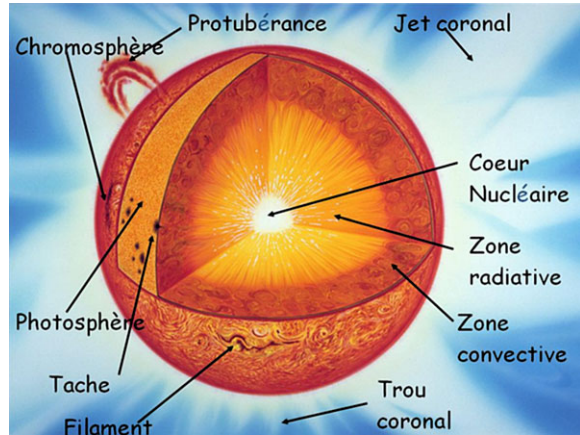
Fig. 2.1 Cartoon showing a
cut into the solar atmosphere

Table 2.1 Main parameters allowing the identification of the Sun

Parameter	Value
Age	4.5 Gy
Radius	696 000 km
Mass	1.99×10^{30} kg
Composition	90 % H and 10 % He
Average density	1 410 kg m^{-3}
Surface gravity	274 m s^{-2}
Escape velocity	618 km s^{-1}
Luminosity	3.9×10^{23} kW
Surface temperature	5780 K
Color temperature	6200 K
Sideral rotation period	25 d at equator; 31 d at poles, which means a differential rotation
Average mass loss	10^9 kg s^{-1} or 10^{-14} Ms year^{-1}

is shortly described in the sixth part. We finally conclude in addressing the current
and future work on the above-mentioned issues.

2.2 Some Properties of the Sun

The properties of this G star are summarized in Table 2.1.

Its general structuring is shown in Fig. 2.1, where one easily distinguishes the
three internal layers below the surface: the core where thermonuclear reactions take
place, the radiative zone where energy is transported through γ photons, and the
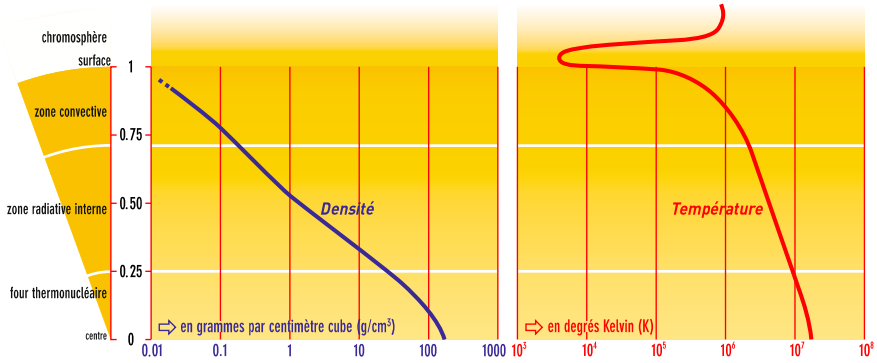convective zone where convection transports the blocked energy. The layers above

Fig. 2.2 The two figures display the run of log(density) (*left-hand side*, in g cm^{-3}) and temperature (*right-hand side*, in K) versus (*in ordinates*) the distance to Sun center normalized to the solar radius. The temperature variation has been extended above the surface in order to show the high coronal temperature

Fig. 2.3 Close-up of the variation of temperature and density below and above the solar surface. Courtesy E. Marsch
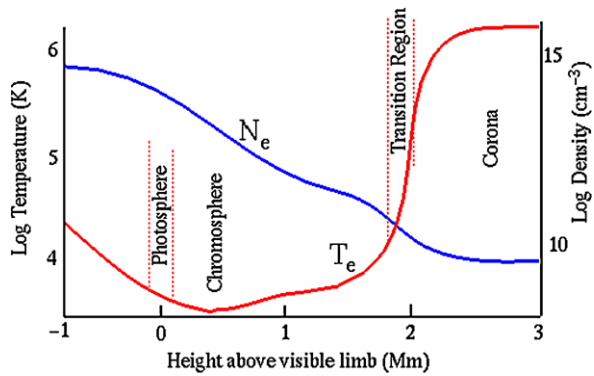
are the photosphere where the visible photons come from, the rather inhomogeneous chromosphere, and a strongly heterogeneous corona.

Average density and temperature values are displayed in Fig. 2.2, essentially in the solar interior. Huge decreases of density and temperature from the solar core to the surface are noticeable, but an increase of temperature has been sketched above the surface. Actually, a close look at the regions slightly below and above the surface (Fig. 2.3) clearly shows a strong temperature jump (of the order of 10^6 K) from the top of the chromosphere to an outer layer located a few hundred km above. This jump characterizes a region called Chromosphere Corona Transition Region or CCTR. This is the well-known coronal paradox which raises the issue of the stealthy heating of the corona.

Before returning to this issue, it is useful to provide a few figures concerning the spatio-temporal scales which are relevant in the outer atmosphere. We know that the solar radius is 700 000 km hereafter expressed as 700 Mm. The typical size of

the granulation (i.e., the surface manifestation of the convection) is 1 Mm, while the supergranulation (which traces the magnetic field concentrations at the level of the chromosphere) has a characteristic size of 30 Mm. Scale heights are 0.1 Mm in the photosphere, 0.3 Mm in the chromosphere, and 50 Mm in the corona. The latter values are smaller than the thickness (or horizontal extension) of the respective layers, a fact to keep in mind when one studies specific features (spicules, fibrils, sunspots, etc.) which depart from the one-dimensional (1D) layering: whatever are the ranges, altitudes and sizes of these features, the overall chromosphere and corona are essentially density-stratified atmospheres.

2.2.1 An Unexplained Solar Region: The Corona

The plasma regime of solar material is essentially collisional at the exception of the corona, which expands into the interplanetary medium. This regime is often characterized by the Knudsen parameter (K = ratio of the mean free path (mfp) to the scale height). The electron mfp in the corona ranges from 5 to 500 km depending on the electron density (10^{16}–10^{14} m^{-3} or 10^{10}–10^{8} cm^{-3}) of the region and altitude. Since the coronal scale height is about 50 Mm (in the low corona), $K \ll 1$ in the low corona. However, this parameter should be taken with much caution since it assumes a fully ionized atmosphere, which may not be the case in the very low corona where material can be partially ionized. Actually, the frontier between collision-dominated and noncollisional plasmas in the high chromosphere and low corona is still debated.

Other physical quantities in the corona are: the electron–ion collision frequency (from 7 to 700 Hz depending on the density), the electron cyclotron frequency (between 3×10^6 and 3×10^8 Hz depending on the magnitude of the magnetic field B: 10^{-4} to 10^{-2} T), electron thermal speed (3900 km s^{-1}), the sound speed (166 km s^{-1}), the Alfvén speed (200 to 2000 km s^{-1}, depending on the magnetic field and density).

In most of the corona (at the exception of prominences), the photon mean free paths, although wavelength dependent, are much larger than the scale height in the corona. From a comparison (Table 2.2) of the convective, thermal, and magnetic energy densities, at the bottom of the convection zone and at the photosphere, it can be seen that the magnetic energy emerges as a major parameter at the surface and in the outer atmosphere. More precisely, the respective thermal and magnetic parameters can be compared in the photosphere, the chromosphere, and the corona (Table 2.3), along with the associated energies and their thermal to magnetic ratio, the β parameter. It can be seen that for the chromosphere and the corona, a large range of values of the magnetic field is provided.

Actually, the magnetic field is more and more heterogeneous in the outer atmosphere from both spatial and temporal standpoints: one finds open (especially at the poles) versus closed (in active regions) fields; and the magnetic field configuration and magnitude change from a period of minimum to maximum activity, as

Table 2.2 A comparison of kinetic, thermal, and magnetic energies at two locations in the solar sphere: bottom of the convective zone and surface. From [34]

Location	$0.7\ R_\odot$	$1.0\ R_\odot$
$\rho v^2/2$	5×10^5	1.5×10^2
$\rho k_g T/\mu$	7×10^{12}	1.5×10^4
$B^2/2\mu_0$	4×10^7 (presumed)	$(0.4\text{–}4) \times 10^4$ (measured)

Table 2.3 Variation with altitude (in fraction of the solar radius) of the temperature, scale height, sound speed, magnetic field, and plasma β. From [34]

	Photosphere	Upper chromosphere	Lower corona	Corona
Height ($R_\odot$)	0.0	$(2\text{–}5) \times 10^{-3}$	$10^{-2}\text{–}10^{-1}$	10^{-1}
Temperature T (K)	6×10^3	10^4	10^6	10^6
Scale height (m)	1.5×10^5	5×10^5	5×10^7	10^8
Sound speed (m s^{-1})	0.8×10^4	1.2×10^4	1.5×10^5	1.5×10^5
Magnetic field amplitude (T)	0.1 (strong)	$(2\text{–}10) \times 10^{-4}$?	$(2\text{–}10) \times 10^{-4}$?	10^{-4}?
Ratio of pressure to magnetic forces	~ 1	~ 1	<1	<1

Fig. 2.4 The real low solar corona, quiet (*left*) and active (*right*) as seen by the EIT imager on SOHO. *Left image*: the quiet Sun at the minimum of activity. Note the general poloidal field structuring. *Right image*: the active Sun at the maximum of activity. Note the general torodoidal fields structuring the plasma
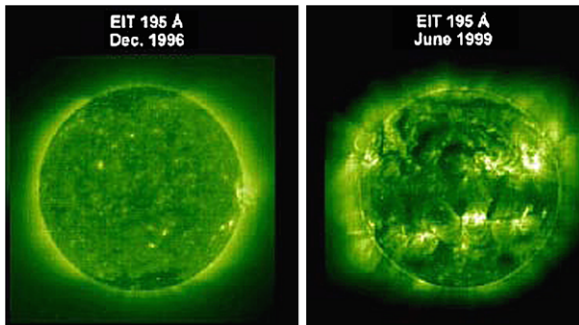
evidenced in the EUV images of Fig. 2.4. In a period of minimum of activity, the magnetic field is radial at the pole (location of decreased density, regions called coronal holes), and its overall structure is poloidal (left). Other areas have locally closed field lines. In a period of maximum of activity (right), one sees a number of local dipoles above and below the equator.

With the concept of large variations of the magnetic field, in terms of space (different structures) and time (solar activity), we now return to the radial variation of the β parameter (Fig. 2.5). The figure not only displays very large spatial (in the horizontal plane) and temporal variations of the plasma β, but evidences a systematic radial trend: between the convective zone and the high corona (where β is lower than 1), there is a regime in the high chromosphere and the low corona where β is much lower than 1. This means that the magnetic field "freezes" the
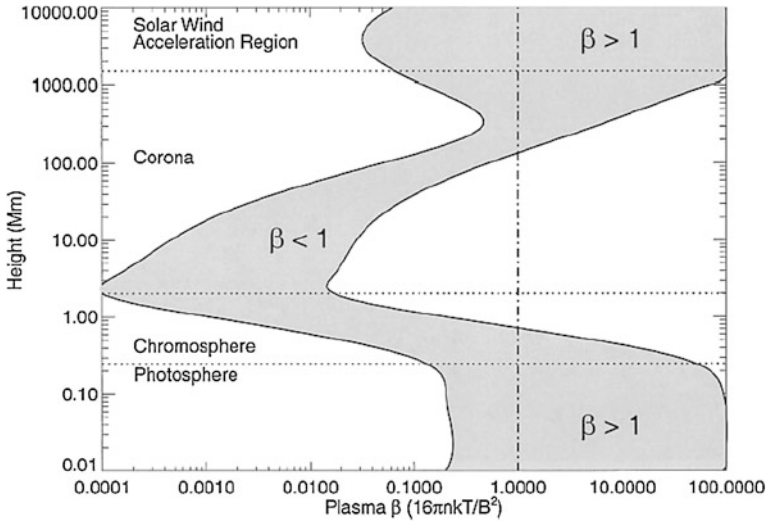
Fig. 2.5 Range of variations of the plasma β (*abscissa*) versus height in the solar atmosphere (*ordinate*). Note that at a given altitude the parameter may vary by more than two orders of magnitude, depending on the structure. The *left and right hand-side curves* correspond to a magnetic field of 0.25 and 0.01 T, respectively ([3] and Courtesy of G. Allen Gary)

plasma, contrary to what happens in the other regions. The situation is also complicated by the fact that the plasma is completely neutral in the lower layers (including the chromosphere), then partially ionized in the transition region between chromosphere and corona (CCTR) to become totally ionized in the corona. It also changes from a very collisional nature in the deep layers (up to the chromosphere) to a non-collisionality in the corona. This change occurs in the regions where β is lower than 1 and the plasma is partially ionized. This means that the plasma is not only dependent of the solar structure studied (we will not go through the whole solar zoo) but also on the degree of filamentation of the plasma which is thought to be beyond the limit of present observational capabilities (about 0.1 arcsec or 70 km at the Sun). For instance, it could happen that a plasma thought to be fully ionized and noncollisional is actually concentrated in small patches where densities are high enough to allow partial ionization and high collisionality. Until now, we focused on the "low corona" (say a hundred Mm above the solar surface) which is accessible to sophisticated remote-sensing techniques (X-ray, EUV, UV imaging, and spectroscopy). Farther out (up to a few solar radii), white-light coronagraphy and UV spectro-coronagraphy (on SOHO and STEREO) have provided a wealth of information, not only on the electron density but also on the electron, proton, and other species temperatures parallel and perpendicular to the magnetic field, to be discussed later.

From these various data, one can try to define a quiet Sun corona (Fig. 2.6, which displays average values of the electron density and temperature up to 10 solar radii
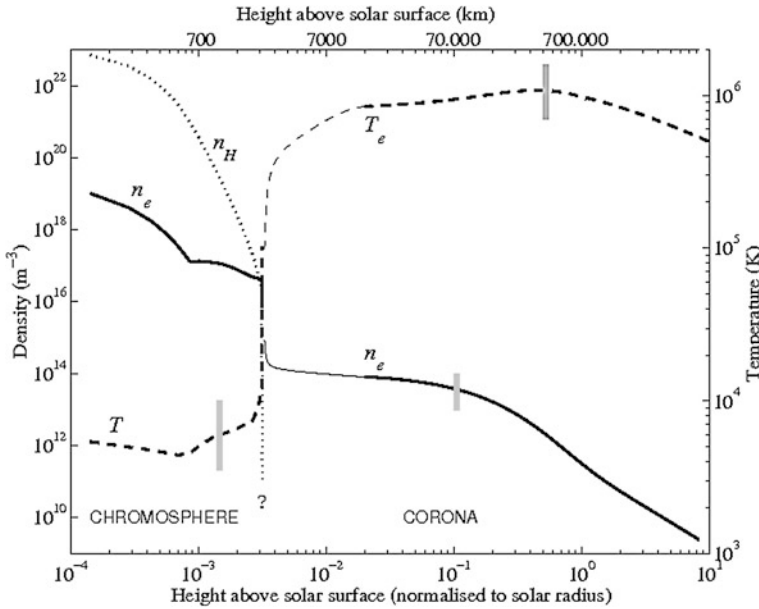
Fig. 2.6 A model of the quiet Sun corona extending up to about 10 solar radii. The altitude marked by an abrupt decrease of density and increase of temperature corresponds to the highly heterogeneous CCTR. From [35]

above the solar surface). The main feature of this figure is the increase of (electron) temperature with altitude up to about 2×10^6 K, some plateau, and a decrease above about one solar radius. With the advent of the STEREO mission, the two Heliospheric Imagers (HI) have been providing images much farther, which allow one to detect moving features in their fields of view. Above about 60 solar radii, the essential information comes from in situ measurements which directly provide most physical quantities (including the full magnetic field vector) but, obviously, in very localized space-time domains, much smaller than the size of the expanding solar structures.

As far as the active corona is concerned, it is still more difficult to build an average model. An example is given by Fig. 2.7 (see also Fig. 2.4, right), where eclipse and coronagraphic images, obtained in the increased phase of activity of Cycle 23, have been adjusted and show radial streamers all around the surface along with a CME in the North-East quadrant (recall that East is on the left). The loci of increased intensity correspond to increased electron density (along the line-of-sight) and also trace the magnetic field lines. These lines are mostly open above about 5 solar radii and consequently suggest the presence of outward flows.

Fig. 2.7 Composite of two
white-light images obtained
on 11 August 1999: the
internal one during an eclipse,
the external one with
C2/LASCO/SOHO. Courtesy
S. Koutchmy (Institut
d'Astrophysique de Paris (F))
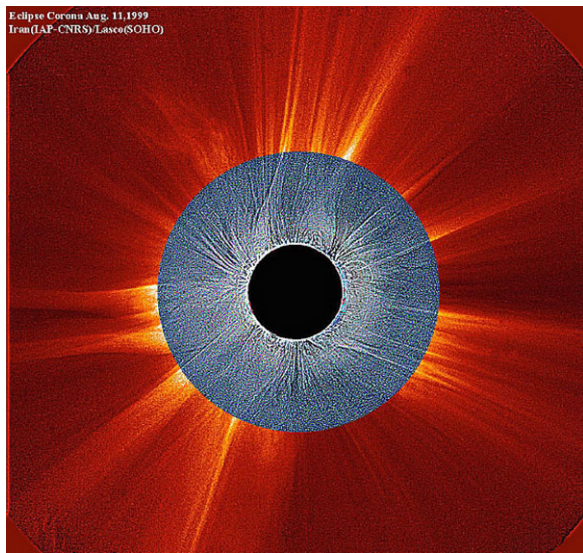
2.2.2 A Simple Derivation of the Coronal Temperature

We first write the energy balance equation between the radiative losses W_R and the conductive flux with the standard notation (q is the conduction factor):

$$\frac{q}{r^2}\frac{d}{dr}\left(r^2 T^{5/2}\frac{dT}{dr}\right) = W_R. \tag{2.1}$$

W_R is given by the equation

$$W_R = n^2 F(T) W\ \mathrm{m}^{-3} \tag{2.2}$$

with n the density and the $F(T)$ variation of radiative losses with temperature as shown in Fig. 2.8, easily parameterized with a set of power laws.

Since the radiative losses are proportional to the square of the density which strongly decreases with altitude (as $n \propto R^{-1.96}$, [17]), they can be considered as negligible. Equation (2.1) becomes

$$\frac{d}{dr}\left(r^2 T^{5/2}\frac{dT}{dr}\right) = 0, \tag{2.3}$$

which becomes the equation

$$\frac{d}{dr}\left(T^{5/2}\right) = \frac{\mathrm{Constant}}{r^2}. \tag{2.4}$$

With the reasonable assumption that the temperature goes to 0 at infinity, Eq. (2.4) is easily integrated into the equation

$$T \propto r^{-2/7} \quad \mathrm{or} \quad T(r) = T_{R_0}\left(\frac{R_0}{r}\right)^{2/7}, \tag{2.5}$$
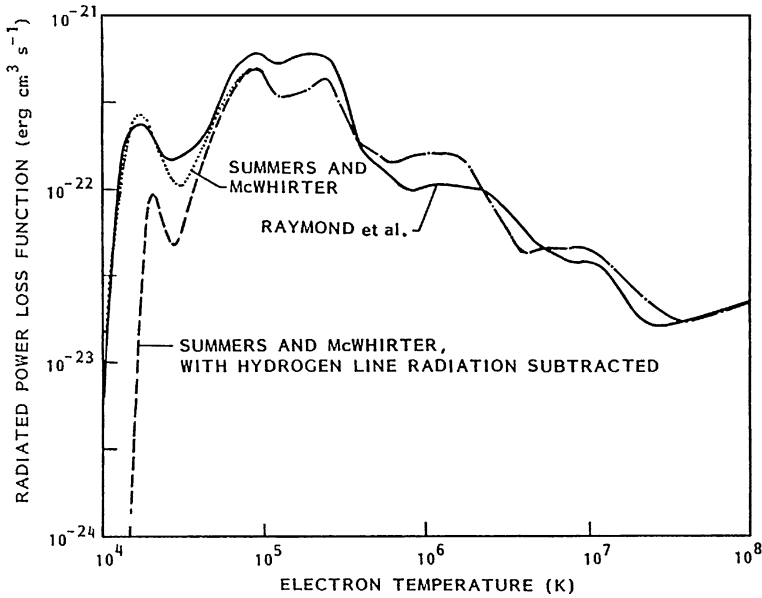
Fig. 2.8 Radiative loss function (in log) vs. temperature (in log) from various authors. The different behaviors at relatively low temperatures (*continuous* vs. *broken lines*) show the importance of H losses in the CCTR and the low corona

where R_0 is the solar radius.

We can now see if hydrostatic equilibrium stands. We write the hydrostatic equilibrium as

$$\frac{dp}{dr} = -GM_0\frac{\rho}{r^2}, \tag{2.6}$$

where G is the gravity constant, M_0 the mass of the Sun, and p the pressure which also follows the gas law $p = 2nkT$.

Then Eq. (2.5) allows us to derive the pressure as a function of radial distance:

$$p = p_o \exp\left(7GM_0r_0\left(\left(\frac{R_o}{r}\right)^{5/7} - 1\right) \Big/ 10 p_o R_o\right). \tag{2.7}$$

All quantities with subscript $_o$ are taken at the solar surface.

When the distance increases to infinity, the pressure goes to a finite value of the order of 10^{-7} Pa. Such a value is higher than the pressure in the interstellar pressure (10^{-13} Pa) by 6 orders of magnitude! One can conclude that the corona cannot be static: as will be shown in Sect. 2.3, material is flowing outwards.

2.3 The Sun and Its Permanent Loss Rate: The Solar Winds

So a wind blows (at least one), a fact which was actually predicted by Biermann as early as 1951 and confirmed by Parker [23] and finally detected/measured with

Fig. 2.9 An image of the Hale-Bopp comet where one clearly identifies two tails: the curved one made of dust and the (*blue*) straight one which is aligned with the comet coma along the solar direction. Its shape and nature (ions) are determined by the blowing solar wind

Mariner 2 in 1962. It was identified as the force acting on comet tails (Fig. 2.9) by Biermann, who wrote of a "solar corpuscular radiation" [6]. It corresponds to an overall (average) mass loss of 10^9 kg s^{-1}.

2.3.1 The Two Kinds of Solar Wind

The two categories have been detected in situ at one AU or farther as in Fig. 2.10. Above most solar regions, one finds a slow wind with a speed of about 400 km s^{-1} while, mainly above the poles, one finds a fast solar wind of about 800 km s^{-1} (up to 1200 or even exceptionally more). This latter result has been beautifully confirmed by the Ulysses probe which went above the poles (or quite) at a distance close to 2 UA. The results are shown in Fig. 2.10, where the wind speed is shown as a vector in the plane perpendicular to the ecliptic. It can be noted that the fast wind is rather steady while the slow wind is variable in time and latitude. It is now well established that the fast wind comes from the above-mentioned low-density regions, the coronal holes. Immediately, a question arises about the high speed and the temperature of these regions.

2.3.2 A First Approach to the Wind Velocity

As shown by Meyer-Vernet [35, Sect. 5.1.1], in the simple adiabatic case, no wind can be produced. On the contrary, in the isothermal case ($\gamma = 1$), it is easily shown that at large distances, the material speed varies as

$$2c_s \sqrt{\mathrm{mod}(\ln r)}, \tag{2.8}$$

where c_s is the isothermal sound speed. Of course, this is a very crude approximation, but one can immediately conclude that since the sound speed is proportional to $\sqrt{T}$, a faster flow should be emitted by a higher-temperature coronal plasma.

Fig. 2.10 Plot of the radial velocity of the solar wind in a plane perpendicular to the ecliptic, superimposed on a composite made of a UV image from EIT/SOHO, a white-light image of the inner solar corona from Mauna Loa, and a white-light image of the corona from C2/LASCO/SOHO. The *blue* (*red*) *regions* correspond to inward (outward) magnetic field, respectively. The velocity has been measured in situ with the SWOOPS instrument aboard the Ulysses probe which was at a distance of 2 AU when above the poles of the Sun. From [20]
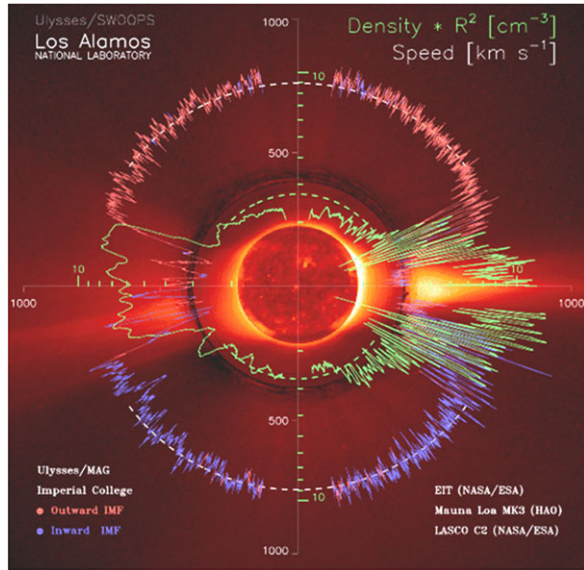
Only with the advent of SOHO and its two EUV-UV spectrometers, called SUMER and CDS, it has been possible to validate (or not) this result. The technique called for sophisticated atomic physics (the so-called Doppler dimming technique described in Sect. 2.3.3) and rather acrobatic measurements since it used two different spectrometers SUMER and CDS on SOHO and necessitated a roll of the spacecraft. The results, shown in Fig. 2.11, are nonequivoqual [8]: the electron temperature in the lower part of polar coronal holes is lower than in the "quiet corona" (i.e., all other closed magnetic regions at the same altitude)! This means that the simple isothermal model mentioned above is invalid and that, in order to build a valid one, one must start by identifying the solar structures and the altitude where the wind comes from.

2.3.3 The "Sources" of the Fast Wind

As far as the fast wind is concerned, the source has been identified as coronal holes, but this information is not sufficient for pinpointing the mechanism at work. The detection of velocities is usually made through the Doppler effect (spectral line shift), but when observing polar coronal holes, the projected velocity along the line-of-sight (LOS) is so small that the line shift is difficult to detect.

Another technique (the "Doppler dimming") is possible but can be worked out only at relatively high altitudes (see below). However the direct Doppler technique has been successfully applied to the lower boundaries of polar coronal holes where projection effects are minimized.
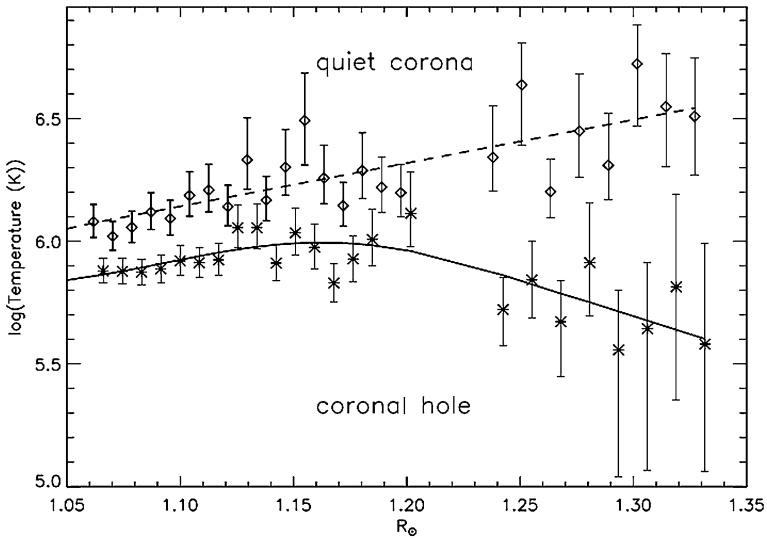
Fig. 2.11 Variation of the electron temperature (in log scale) with the altitude normalized to the solar radius [8]

Fig. 2.12 The green image was obtained in the Fe XII line at 19.5 nm with EIT/SOHO. It shows the coronal hole border where the SUMER profiles of Ne VIII (77 nm) have been obtained in and out the coronal hole. The blueshifts (coded in *blue*) correspond to outward flows, while the redshifts (coded in *red*) correspond to inward flows. Note that the strongest outflows in the coronal hole correspond to areas where contiguous chromospheric networks (delineated in *black*) converge [13]
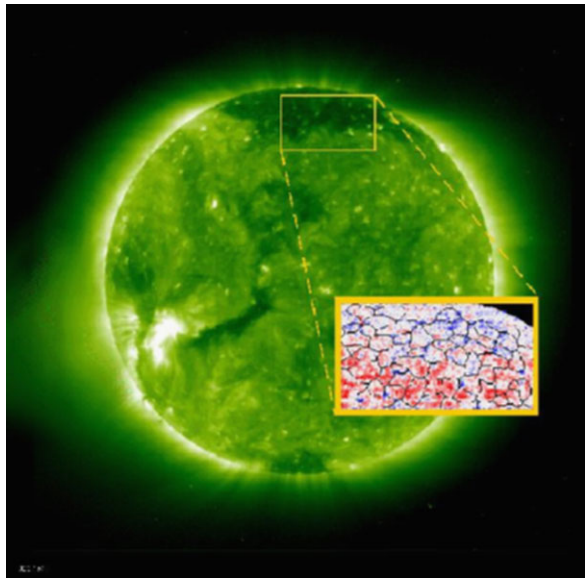
Using SUMER profiles of the UV Ne VIII line at 77 nm and formed at 6×10^5 K, Hassler et al. [13] were able to detect blueshifts of the order of a few km s^{-1} above the contours of the chromospheric network where operates what we called above the supergranulation (Fig. 2.12). So, at the 6×10^5 K level (high in the CCTR), we already have an outflow, but in the coronal hole, this ouflow is stronger at the

Fig. 2.13 EIT and eclipse
images of the South Pole
region where the
spectroscopic SUMER
observations took place. *Top*:
EIT image in Fe IX/X at
17.1 nm, where polar plumes
are well evidenced. *Bottom*:
White-light (eclipse) image
(courtesy J.-R. Gabryl, taken
on 26/02 1998 at 18:33 UT).
The SUMER slit is shown as
a thin rectangle on both
images: since it cuts the solar
limb, the altitude is rigorously
defined. From [24]
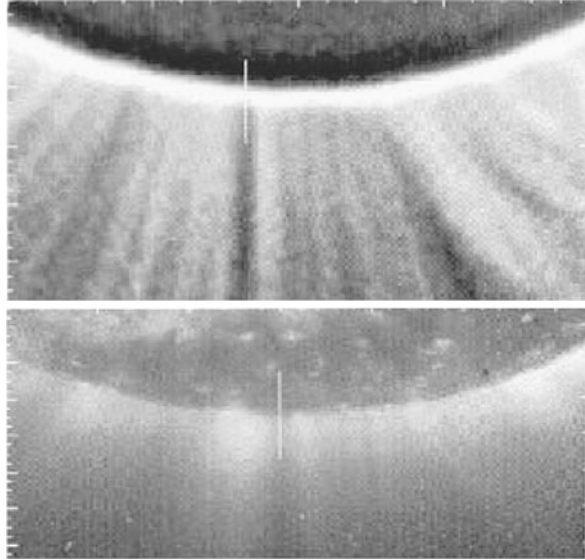
frontiers of the supergranulation pattern. It should be noted that lower values have
been finally obtained by Wilhelm et al. [31].

Higher in the atmosphere, when observing out of the limb, one definitely loses
any possibility of measuring radial flows with the Doppler method. Then, one can
rely on the technique dubbed Doppler dimming initially developed by Noci [22] in
the case where a chromospheric or CCTR line is resonantly scattered by remaining
ions or atoms in the corona. It is then easy to understand that the coronal atoms and
ions only fully absorb the incident radiation if it is not shifted by Doppler effect.
When relatively strong radial flows are at work, these atoms or ions no longer see
the incident line (or only the wings), and the scattered radiation decreases: this is
why this effect is called "Doppler dimming."

This technique has been extensively used by the UVCS/SOHO Team and was
developed in order to take into account the collisional contribution to the radiation,
thereby allowing its use in the very low corona. However, it should be kept in mind
that it requires, amongst others, the knowledge of the electron density. In a rather
unique combined eclipse-SOHO observation (Fig. 2.13), Patsourakos and Vial [24]
were able to derive the density from the eclipse white-light data, and from the ratio
of the O VI doublet at 103.2 and 103.7 nm from SUMER they derived the radial
velocity (Fig. 2.14). At 0.05 solar radius above the limb (or 35 Mm), they found
$67 \, \mathrm{km \, s^{-1}}$, a rather important figure at such a low altitude. Moreover, their spectro-
scopic measurement took place in a "void" region between plumes, plumes being
the radial regions of higher density found in coronal holes (Fig. 2.13). The authors
could then claim that the fast wind originates from the "interplumes." The authors
could also derive: $T_e = T_i = 0.9$ MK and $n_e = 1.8 \times 10^7 \, \mathrm{cm^{-3}}$ in this interplume
region.

Fig. 2.14 Variation of the OVI 103.2 to 103.7 intensity ratio with the radial outflow velocity. The *horizontal line* corresponds to the measured value. From [24]
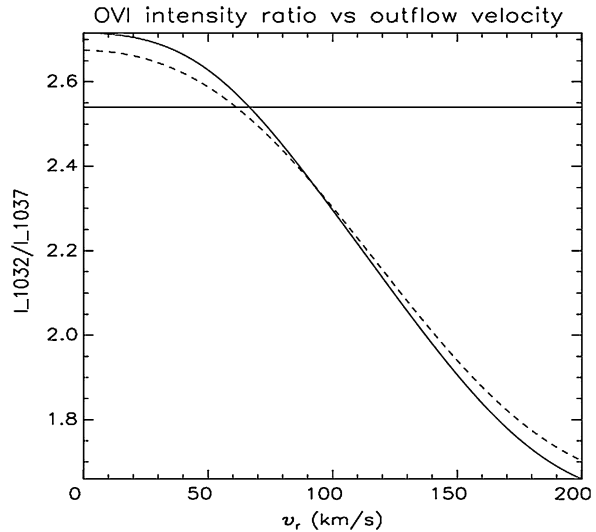
The issue of the plumes vs. interplumes origin of the fast wind is the subject of an ongoing hot debate (see [10]). Actually, the diagnostic is made difficult by line-of-sight (LOS) effects as discussed in [10], who suggest that some plumes could result of the superposition of network boundaries when seen out-of-limb. In view of the Hassler et al. results (outflows at network boundaries), this could explain why fast wind is also detected in plumes (for the most recent review, see [32]). Other sources are proposed such as small-scale ejecta and spicules of type II, now suspected to be the source of coronal heating [9]. Expanding "Funnels" have also been proposed by Tu et al. [28]: in these structures, high-frequency Alfvén waves (<10 kHz) would start in the chromosphere. A nice feature of this mechanism is that it could explain the "FIP" effect (overabundance of elements with First Ionisation Potential (or FIP) <10 eV) in the solar wind.

2.3.4 The "Sources" of the Slow Wind

As shown in Figs. 2.10 and 2.15, at the solar minimum of activity, the slow wind is confined in low-latitude regions with multipolar (consequently closed) magnetic field. So it has been suggested that the slow wind would be initiated from the boundary between the dominant coronal hole and the current sheet(s) resulting from the complex magnetic field [5, 26]. It is true that strong outflows have been found at the boundary between coronal hole and active region [4, 25], but "open" field lines could actually be long-range closed lines (as shown in Fig. 2.16 and in [7]). See also [12, 14]. Anyway, this is still an open question.
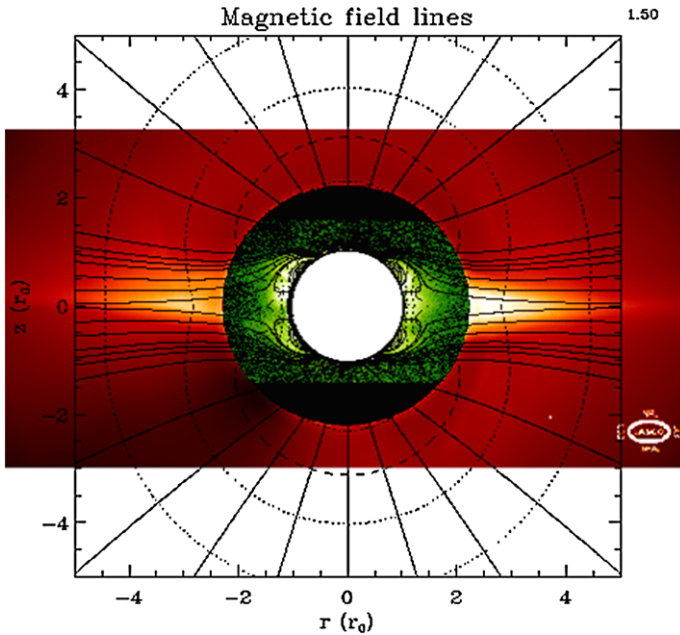
Fig. 2.15 On a montage of C1/C2 white-light images from LASCO/SOHO, magnetic field lines are superposed. The slow wind emanates from regions which are supposed to be closed fields [5]

2.4 Fluid Models of the Wind

These models are based upon a set of assumptions:

1. The thermal (electron) conductivity is given by the expression

$$\kappa \sim \frac{3}{2} n k_B v_{\text{th}} l_f, \tag{2.9}$$

   where the symbols have the usual meaning (n density, k_B Boltzmann constant, v_{th} the electron speed, and l_f the mean free path). Equation (2.9) becomes

$$\kappa \sim 10^{-11} \times T^{5/2} \ \text{W}\,\text{m}^{-1}\,\text{K}^{-1}. \tag{2.10}$$

2. The mean free path (l_f) is much smaller than the plasma variation scale. This is obviously verified in the very low corona where $l_f \sim$ a few 100 km, but at 1 A.U. ($n \sim 5 \times 10^6$ m^{-3}; $T \sim 10^5$ K), $l_f \sim 1$ A.U.! Moreover, l_f varies as v^4, so $l_f(3v) \sim 100 l_f(v)$, which means that the assumption is no longer valid for velocities in the high wing of the distribution.
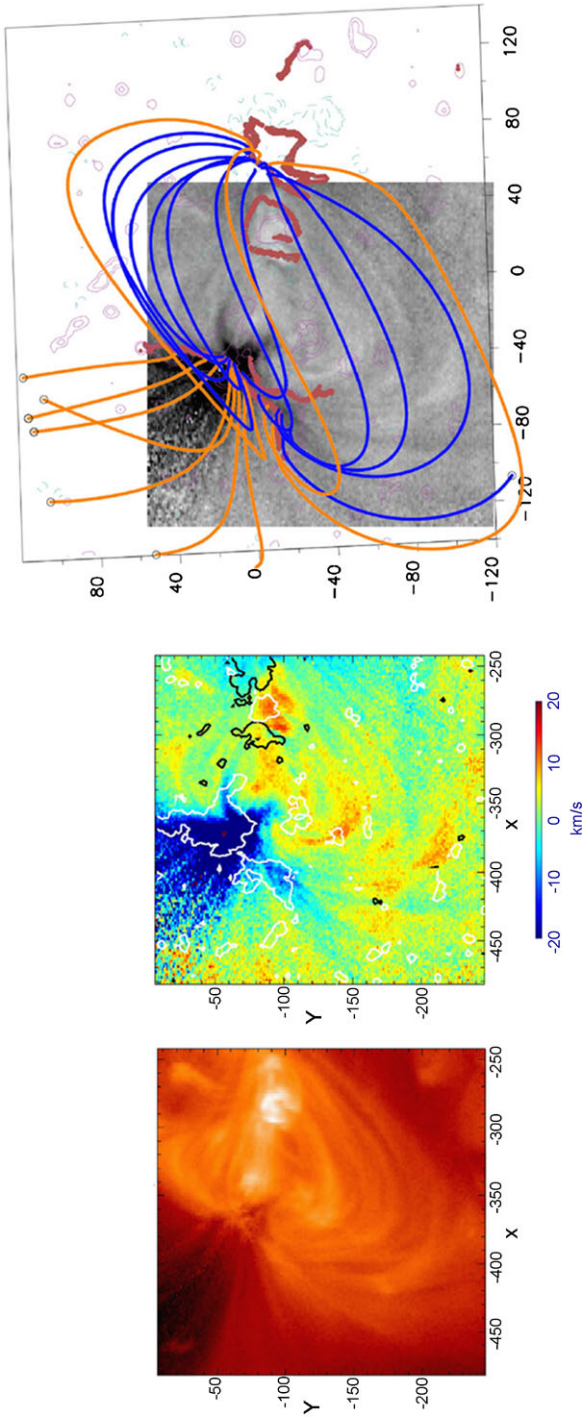
Fig. 2.16 Plasma flows and magnetic field lines in and between the two active regions AR10942 and 10943. *Left image*: FeXII 19.5 nm intensity (EIS/Hinode). *Middle image*: Velocities derived from FeXII Doppler shifts in the usual blue and red color convention (EIS/Hinode). *Right image*: extrapolated magnetic field over velocities field (FeXII Doppler shift with a black and white convention) [4]. All axis of these figures are in arcsecs

Fig. 2.17 *Top*: variation of the wind speed with altitude (in 10^3 Mm up to the Earth orbit) for different values of the temperature (from [23]). *Bottom*: wind velocity as measured with the so-called "blob" technique as a function of altitude (up to 25×10^3 Mm). (The technique consists in identifying and following pieces of plasma (or blobs) during their expansion) (from [27])
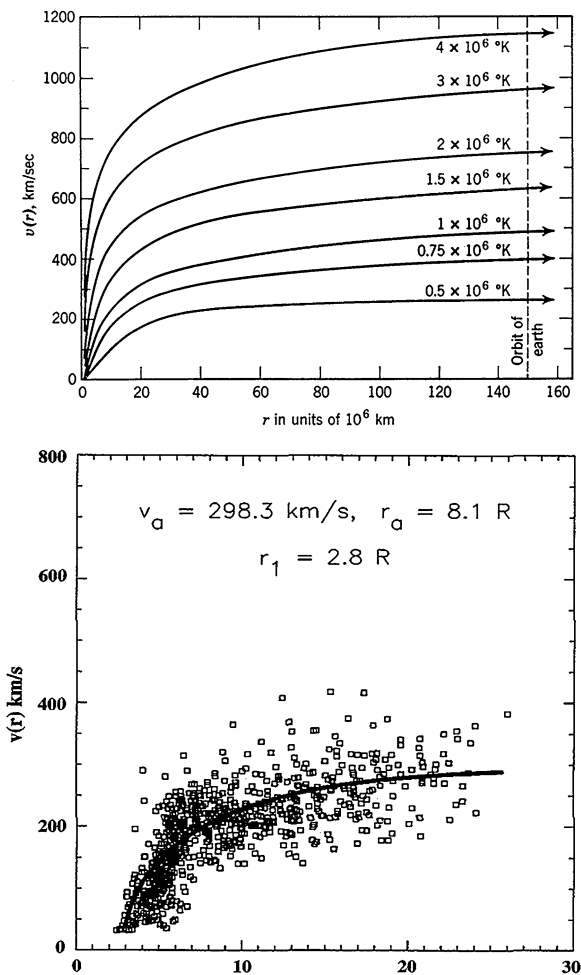
2.4.1 The Isothermal Parker Model

From the laws of conservation of mass and momentum one can derive the equation

$$(V/c_s)^2 - \ln(V/c_s)^2 = 4\big(\ln(r/r_c) + r_c/r\big) + \text{Constant}, \qquad (2.11)$$

where c_s is the sound speed, and r_c the critical distance defined by $r_c = GM/(2c_s^2)$.

A positive velocity gradient $dV/dr > 0$ implies that for $r < r_c$, the flow is subsonic, while for $r > r_c$, it is supersonic. For the Sun, $c_s = 140$ km s^{-1}, $r_c = 4.5$ R, and the mass loss is found to be 1.6×10^9 kg s^{-1} (about the measured value).

The Parker solution can be compared to measurements made by Wang et al. [30] and Sheeley [27] from isolating plasma "blobs" in the slow wind and following their motions (Fig. 2.17). The overall agreement is rather good, at least in the observed

Fig. 2.18 The four sets of
solutions (I, II, III, IV) of the
(signed) Mach number as a
function of radial distance.
The stationary outflow
solution is marked in thick
line and is noted *W*
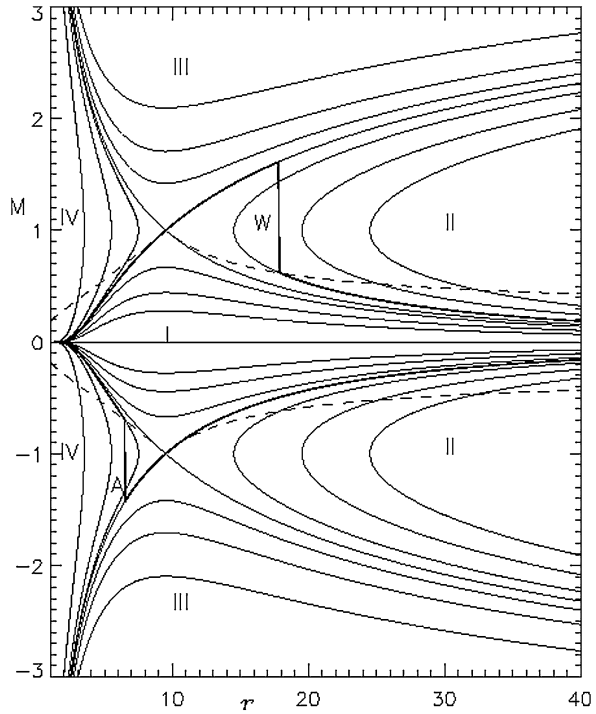
regions (below 10^3 Mm). Much farther but below one AU, the only (in situ) mea-
surement was performed by Helios, and a velocity of about 300 km s^{-1} was found.
However, the model is not satisfactory because of the low "constant" temperatures
implied (less than 10^6 K) and definitely does not represent the fast wind, which
would require, as we have seen, a too high temperature.

2.4.2 Solving the Bernoulli Equation [36]

The four sets of solutions (I, II, III, IV) in terms of the Mach number $M = V/c_s$
are shown in Fig. 2.18 as functions of radial distance normalized to the solar ra-
dius. Note that the graph also takes into account the accretion process (lower part
of the figure where $V < 0$). If one adopts the right and unique pressure values at
the lower boundary (the "surface") and at infinity, one has a stationary outflow so-
lution (denoted W) with a subsonic breeze (which matches the observed velocity)
until, above about 10 solar radii, the wind becomes supersonic. This supersonic flow
leads to a shock below about 20 solar radii (which allows for a low terminal pres-
sure). A thorough discussion why other solutions are discarded can be found in [35,
Chap. 5].

Fig. 2.19 Distribution of the electron velocity. The parallel and perpendicular velocities are compared to the Maxwellian distribution. From [35] and courtesy I. Zouganelis
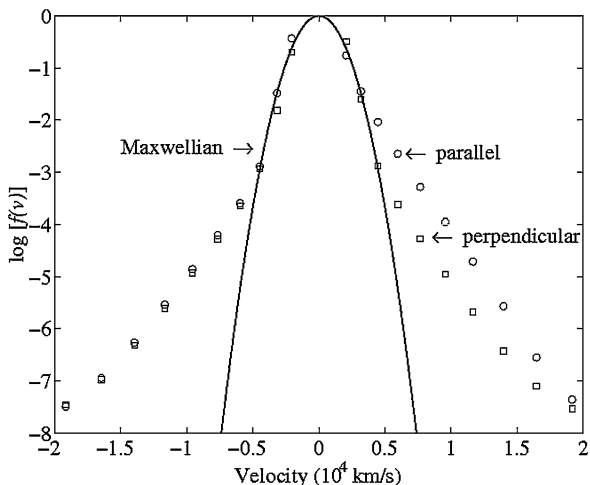
2.4.3 The Fast Wind and the Fluid Models

As we have seen, there is, for the fast wind, a temperature issue: in order to have a fast wind with a $T < 10^6$ K corona, one needs to deposit additional momentum in the flow. Several tricks have been proposed:

- Polytropic approximation with $\gamma < 5/3$, but why?
- Two-fluid model (in order to take into account the fact that $T_p > T_e$ as observed at increasing distances from remote-sensing UVCS/SOHO to in situ Ulysses measurements);
- Alfvén waves in a nonradial expansion geometry: with frequencies up to 10 kHz generated in the chromospheric network, it implies supersonic speeds in the very low corona.
- Ion gyroresonance (which couples incident high-frequency waves with ion gyration), derived from UVCS/SOHO line profiles measurements perpendicular to the open magnetic field and showing a strong anisotropy of line widths [16].
- And so on...

As said by N. Meyer-Vernet in her book (Basics in the Solar Wind), solar physicists have devised "more and more ingenious schemes reminiscent of the Ptolemaic system...". The main handicap of fluid models is that by definition they cannot take into account the fact that observed particles distributions are far from Maxwellian (or bi-Maxwellian), e.g., the electron distribution of Fig. 2.19 (courtesy I. Zouganelis) or the protons distributions found with the Helios mission in the fast wind at about 60 solar radii (Fig. 2.20). The proton distribution is not only non-Maxwellian but also highly anisotropic [18]. In view of these deficiencies, more and more physicists have turned to models which describe the velocity distributions and their various moments: density, mean velocity, etc. But can we speak of a Copernician revolution? See below.
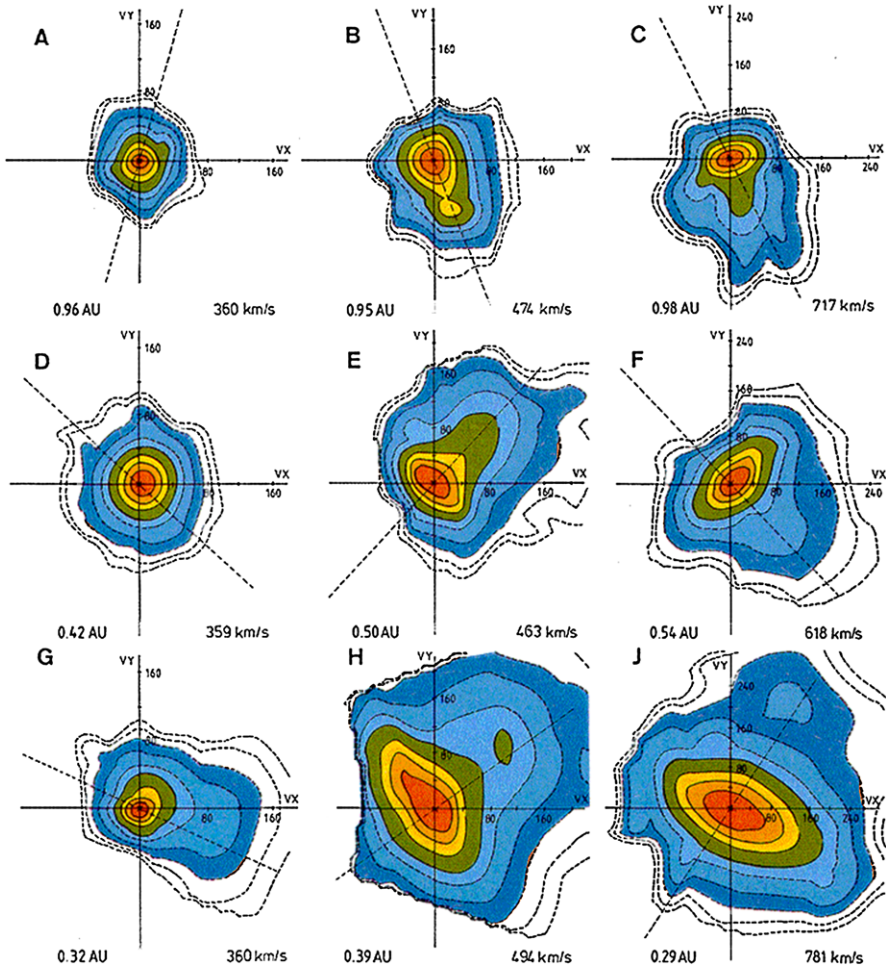
Fig. 2.20 *Top*: Angular distribution of protons as measured by Helios with variable distances from the Sun. The distance varies from 1 AU (*upper left-hand image* labeled **A**) to 0.29 AU (*lower right-hand image* labeled **J**). *Bottom*: Proton distribution at increasing distances from the Sun as measured by Helios. Note the strong asymmetry in the wings (from [18] and [35])

2.5 The Fast Wind and the Kinetic/Exospheric Models

2.5.1 The Kappa Distribution

The distribution is described by the equation

$$f_n(v) \propto \left[1 + \frac{v^2}{\kappa v_{\text{th}}^2}\right]^{-(n+1)}. \tag{2.12}$$

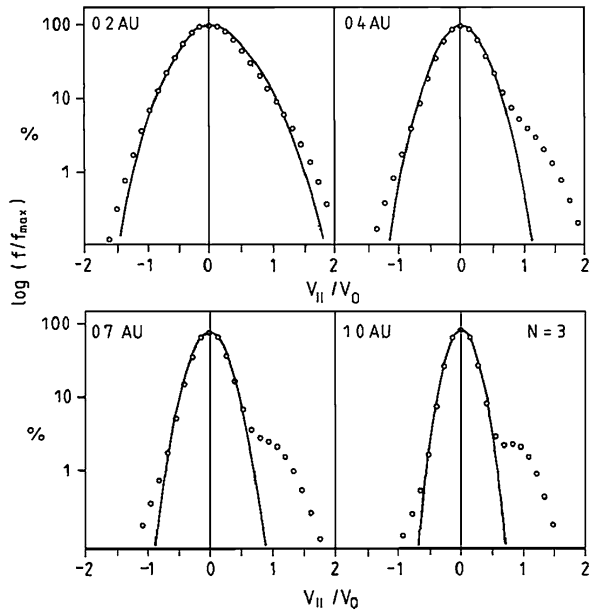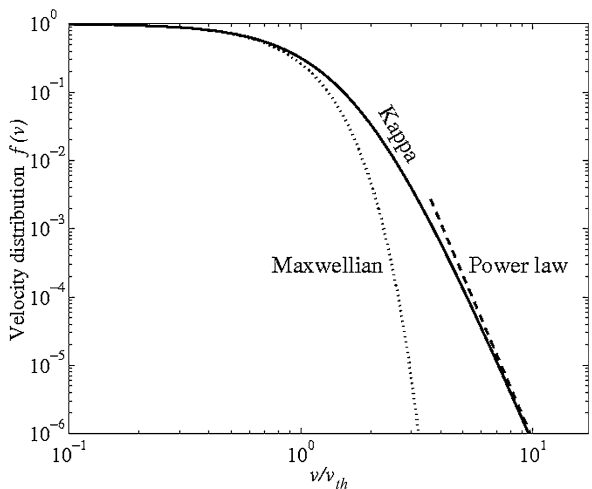**Fig. 2.20** (Continued)

Fig. 2.21 The $\kappa = 3$ distribution as a function of v/v_{th} compared to Maxwellian and power law distributions. From [35]

It is nearly Maxwellian at low speeds and decreases as a power law at high speed (Fig. 2.21). The power law part where energy accumulates at a rate proportional to itself reminds of the flare to nanoflare energy distribution. Could it be the same "nanoscale" phenomenon?

2.5.2 Exospheric Models

The electrons, being light, tend to concentrate in the outer coronal regions, contrary to protons which, being heavy, drift into the inner regions. This leads to the formation of an electrostatic potential $\Phi_E(r)$. Expressing the total electron energy, one gets the equation

$$M_e v^2/2 - e\Phi_E(r) = \text{Constant}. \tag{2.13}$$

Introducing $v_E = \sqrt{2e\Phi_E/m_e}$, one can compare v and v_E. When $v < v_E$, electrons are trapped. If $v > v_E$, electrons move outward to infinity. But an excess of escaping electrons increases the potential which rises the electric field which increases the wind speed, etc.

So it seems appropriate to improve the model, e.g., introducing the invariants of motion leads to a very small cone of escaping electrons. One can also include collisions and wave–particle interactions. Actually, building a full model requires putting the boundary conditions in the chromosphere where … radiative losses are important, the heat conductivity is not very well known, the magnetic field energy dominates (plasma $\beta \ll 1$), but where the magnetic field is not measured, where the geometry (including the introduction of a filling factor) is complex and the temporal variations important. One can easily imagine that it is a formidable task for solar physicists.

Finally, one can compare the situation of our Sun and solar-type stars where hot coronae are associated to diluted, hot and fast winds to giant ($T = 10^5$ K and $v = 200$ km s^{-1}) and supergiant stars ($T = 10^4$ K and $v = 10$ km s^{-1}), where winds are denser and cooler. Broadly speaking, the "Parker" law is satisfied. Radiation-driven winds are of a completely different nature and out of the scope of this presentation.

2.6 The Sun and Its Activity-Related Plasma Losses

Not only the Sun loses mass in a continuous way but also episodically with three types of events: flares, erupting prominences (EP), and Coronal Mass Ejections (CME), see e.g. [38] and [41]. The three features are shown in Figs. 2.22, 2.23, and 2.24, respectively. A flare (Fig. 2.22) can be defined as a strong brightness enhancement in all wavelengths, especially in the UV and X-rays, which means that the plasma reaches very high temperatures (a few 10^7 K). An eruption of prominence is the lift-up of cool material (less than 10^4 K), which sometimes, but not always, leaves definitely the solar corona where it was initially embedded (Fig. 2.23). A CME is the ejection of cool and hot material toward the interplanetary medium and can only be observed with a coronagraph, very often through a technique of subtracting two consecutive images (Fig. 2.24). Flares, EPs, and CMEs all imply large energies (radiative, thermal, etc.), but what about their mass losses, which is the today topic?

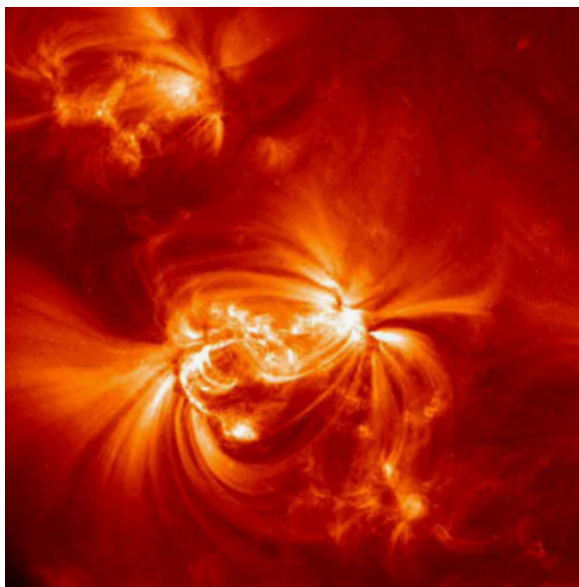**Fig. 2.22** Flare observed in the EUV by TRACE

Fig. 2.23 Eruption of a prominence (EP) observed in the He II line 30.4 nm (formed at about 70 000 K) by EIT/SOHO

Fig. 2.24 Coronal Mass
Ejection (CME) observed by
the C3 coronagraph of SOHO
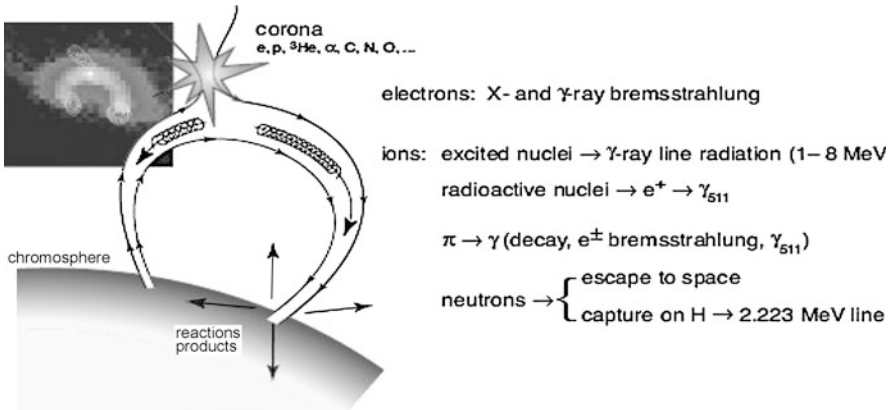at about ten solar radii. Note
the "tennis racket" shape of
the CME

corona
e, p, ³He, α, C, N, O, ...

electrons: X- and γ-ray bremsstrahlung

ions: excited nuclei → γ-ray line radiation (1– 8 MeV
radioactive nuclei → e⁺ → γ₅₁₁

π → γ (decay, e± bremsstrahlung, γ₅₁₁)

neutrons → { escape to space
              capture on H → 2.223 MeV line
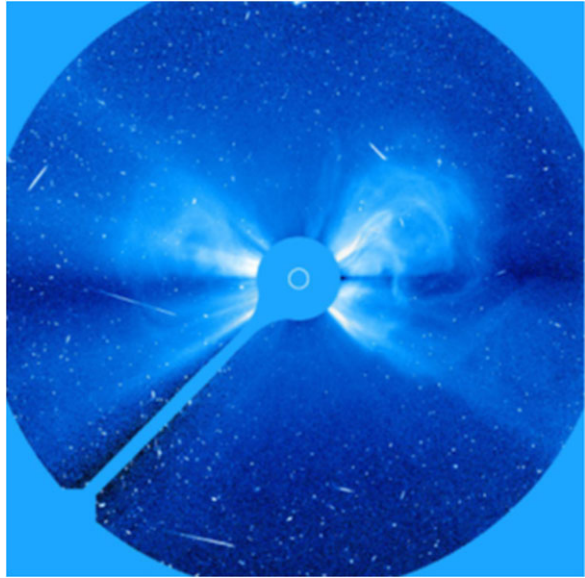
chromosphere

reactions
products

Fig. 2.25 Cartoon depicting the three main features of a flare: acceleration of particles, precipita-
tion on the surface (and associated heating), and escape of SEP cartoon taken from Fig. 2 of the
SMESE proposal [29] and adapted from [21] and [19]

2.6.1 Flares

The energy release is typically of the order of 10^{26} J, an energy which goes into
heating, particle acceleration, the release of Solar Energetic Particles (SEP), and
(sometimes) a CME. Let us discuss the cartoon of Fig. 2.25. The main ingredi-
ents of the common flare scenario can be found: some disruption (magnetic re-
connection?) occurs in a loop-like magnetic structure, and particles are accelerated
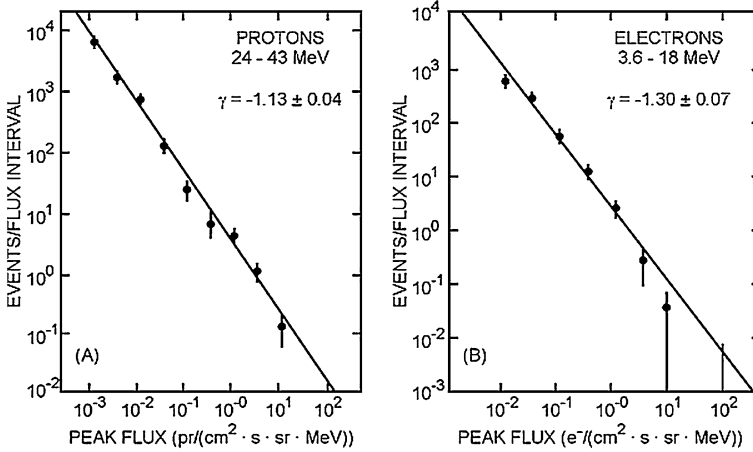
Fig. 2.26 Distributions of (IMP-8) SEP peak intensities of $24 < E < 43$ MeV proton events (*left*) and $E > 3$ MeV electron events (*right*). At higher energies (not shown), the slope of the power law increases in modulus. Taken from Fig. 19 of [15]

(magnetic reconnection?) at high energies. Part of them "fall" into the solar surface (emitting bremsstrahlung radiation) and impinging on the dense chromosphere and photosphere, they heat, through Coulomb collisions, the local plasma which intensely radiates (it "flares"). The other part, which is of interest here, leaves the Sun and propagates in the interplanetary medium. These SEPs have a typical spectrum of Fig. 2.25. They carry a mass less than 10^4 kg s^{-1} for an event duration of less than a few hours. This is orders of magnitude smaller than the solar wind in one second. But, as shown by Fig. 2.26, they carry energies per nucleon higher than one MeV. Finally, since the high chromosphere and low corona are severely perturbed, the new magnetic configuration can lead to plasma ejections such as CME. Actually SEPs are often associated with CME. Of course, their propagation times are widely separated: about an hour for protons with energies of 20 MeV and about two days for CME propagating with a speed of about 800 km s^{-1}.

2.6.2 Eruptive Prominences

A prominence consists in cool ($T \sim 10^4$ K) and dense (10^9–10^{11} cm^{-3}) material suspended and confined in the corona. It lies upon a magnetic inversion line in such a way that the material is prevented to fall by the (horizontal) magnetic tension. Its mass $M \sim 5 \times 10^{12}$ kg is known within a factor 10 (at least) because it depends on the volume (i.e., the morphology of the filament/prominence). For a complete overview, see [39] and [40]. Since $M_{prom} \sim M_{cor}$ or less, prominence eruptions are not frequent enough to "feed" the corona. How much material actually leaves the Sun? The set of movies obtained with SDO and STEREO easily shows that not all
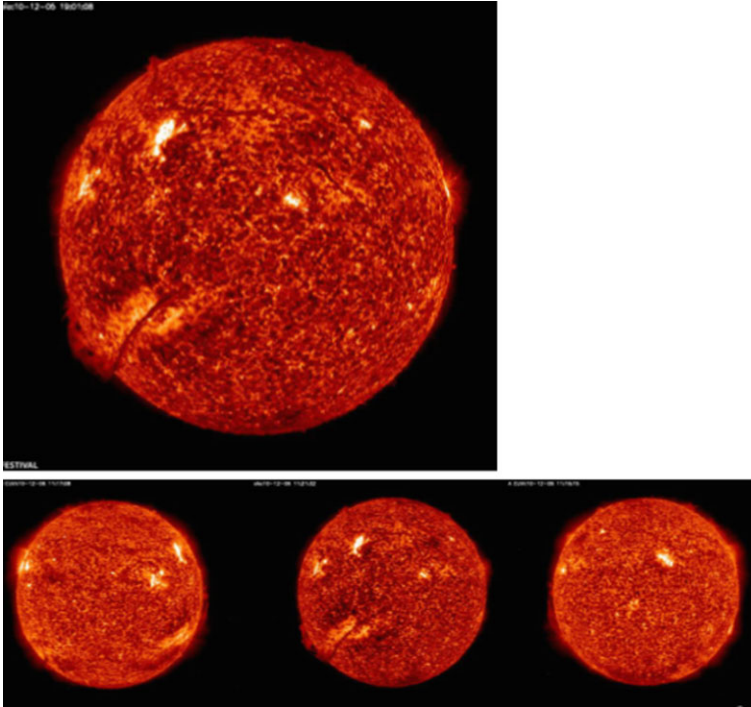
Fig. 2.27 Quasi-simultaneous movies obtained in the He II 30.4 nm line by the EUVI imagers on the STEREO A and B probes and the AIA imager on SDO on 6 Dec. 2010. *Top*: The large images, taken at a cadence of about 12 s, show part of the EP at the South-East (*lower and left*) part of the solar image. *Bottom*: The set of three movies come respectively from STEREO B (*left*), SDO (*center*), and STEREO A (*right*). The STEREO B images (at South-West) allow one to observe the leg of the EP invisible with SDO. (Movies available to the public, courtesy STEREO and SDO Teams)

material is carried out and that some material flows back toward the feet of the EP (Fig. 2.27). These are really unique observations made when the EUV imagers of the STEREO B (and A) and SDO were separated by nearly 90°. The evaluation of the respective parts of the CME leaving the Sun and returning to the Sun is not straightforward because there is no simple law relating the emissivity of the He II (30.4 nm) line and the density of the material (a usual problem in remote-sensing measurements).

2.6.3 Coronal Mass Ejections

The mass involved in a CME, which comes essentially from the EP material, is in the range 10^{12}–10^{13} kg. Of course, it is important to take into account the frequency of such events. At minimum of activity, there are two events per week on average: with
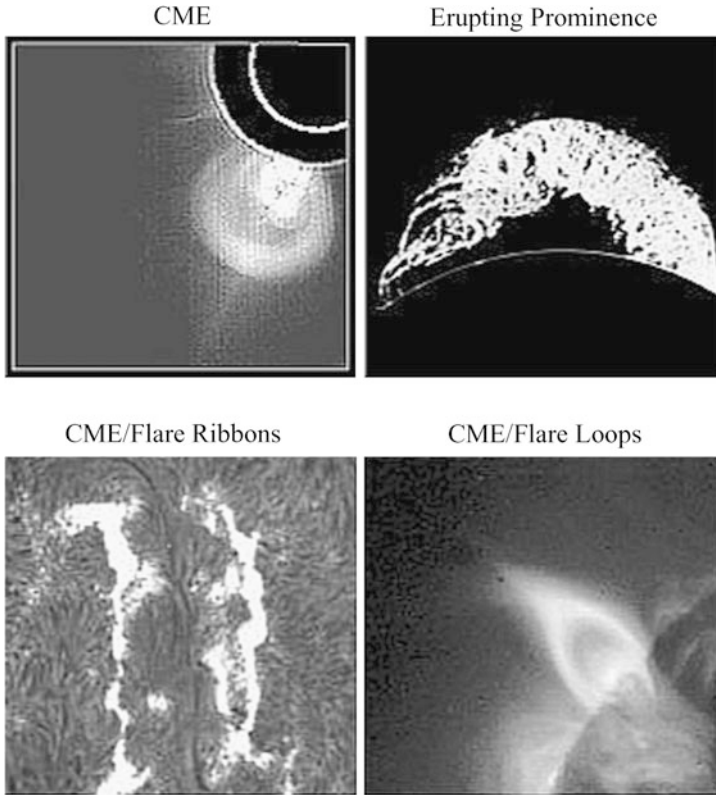
Fig. 2.28 The four images display a CME and an EP (*top row*) and two flare structures (flare ribbons and flare loops) associated with the CME. The different features are not as disparate as taken at face value. They can be unified with the cartoon of Fig. 2.29 (from [37])

a rate of 3×10^6–3×10^7 kg s^{-1}, this is much less than the Solar wind. At maximum of activity, with two events per day, the rate becomes 3×10^7–3×10^8 kg s^{-1}, still orders of magnitude smaller than the Solar wind. As for the kinetic energy, with a velocity ~ 1000 km s^{-1}, one gets 0.5×10^{24}–0.5×10^{25} J, smaller but of the order of flare energy (10^{26} J).

2.6.4 Flares, EPs, and CMEs: Closely Related Phenomena

The different aspects of the three phenomena are well evidenced in Fig. 2.28. The CME and EP (top row) have distinct shapes (sizes, altitudes, etc.). The CME is associated with a flare with its two main features (low row): loops (right-hand side) and ribbons (actually feet of the loops, left-hand side). Is it possible to catch these distinct features within a single process? and who starts first? Figure 2.29 summarizes

Fig. 2.29 The four images displayed in Fig. 2.28 are summarized in a cartoon where the lift-off of the magnetic structure leads to the following time sequence described from right to left: a shock bow in front of a plasma pile-up, followed by a coronal cavity, overlying the cool prominence no longer maintained by magnetic field filling X-ray loops whose activated feet delineate flare ribbons (from [37])
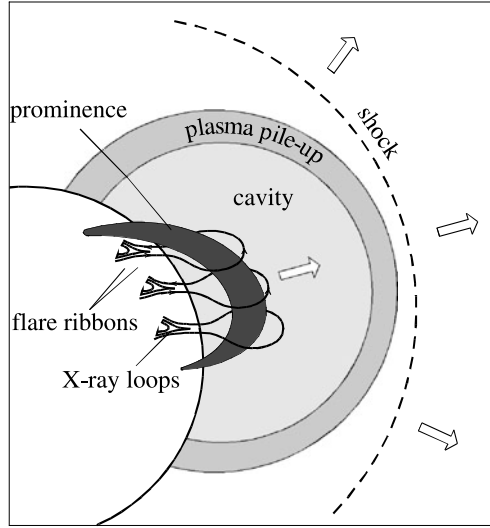

Table 2.4 Typical values of magnetic, thermal, kinetic and gravitational energies in the corona

Energy type	Formula	Value (J/m³)	Parameter values
Magnetic	$\frac{B^2}{2\mu}$	40	$B = 100$ Gauss
Thermal	nkT	0.01	$n = 10^{15}$ m^{-3}, $T = 10^6$ K
Bulk kinetic	$\frac{m_p n v^2}{2}$	10^{-6}	$n = 10^{15}$ m^{-3}, $v = 1$ km/s
Gravitational	$m_p\, n\, g\, h$	0.04	$n = 10^{15}$ m^{-3}, $h = 10^8$ m

the eruption (EP, flare, and CME) in a simple cartoon, without providing the answer but implies a disruption of the magnetic field which is treated in Sect. 2.6.5. This disruption is made possible through the realization that a single energetic process is at work, namely the release of magnetic energy stored in the coronal magnetic field. Table 2.4 [37] shows how the magnetic energy in the lower coronal layers dominates all other energies and can be the energy reservoir, at least in active regions since the adopted value for the magnetic field, 100 G (or 0.01 T) is not the average coronal field! (Also note that the table does not take into account the solar wind kinetic energy.)

2.6.5 Models of Formation of EP and CME

This is a very active field where models flourish for the main reason that the triggering mechanism is still unknown. We focus here on two popular mechanisms and scenario, the flux rope and the break out models. The flux rope model is illustrated by Fig. 2.30 [1]. The left-hand drawing of the field lines shows how a magnetic flux
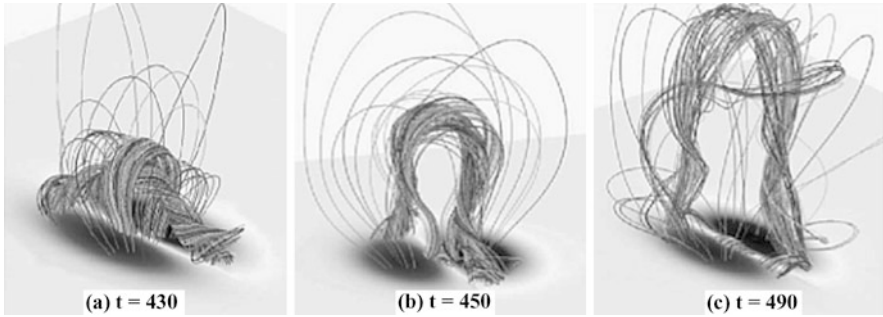
Fig. 2.30 A three-step model of an Eruptive Prominence. *On the left*, one sees a magnetic flux rope (mfr), highly twisted and elongated along the magnetic neutral line, which is lifting up, pushing the magnetic field of the coronal arcades above. The mfr expands (*middle drawing*) while becoming more perpendicular to the neutral line. Finally (*right drawing*), it gets free with a decrease of the twist of the field lines (from [1])

rope (mfr), highly twisted and elongated along the magnetic neutral line, lifts up, pushing the magnetic field of the coronal arcades above. The mfr expands (middle drawing) while its feet are getting closer on both sides of the neutral line. Finally (right drawing), it gets free with a decrease of the twist of the field lines. The timing is not clear in the sense that the mfr could emerge already twisted from the convection zone or emerge far in advance and become more and more twisted because, e.g., of photospheric motions of the footpoints. The break out model (e.g., [2]) is explained in Fig. 2.31 (from [37]). It starts with a quadrupolar magnetic structure (right hand drawings) where the region between the two dipoles is prone to flux rise (top drawing 1 and middle drawing 2). The end of phase 2 sees the appearance of an X-point and magnetic reconnection. Finally, the magnetic configuration (lower drawing 3) includes a plasmoid at the top, a current sheet below, and loops close to the surface. On the left-hand side, the free magnetic energy is plotted vs. time and the three different phases are shown: the free energy first strongly increases and then decreases when the reconnection takes place. Note that the Alfvén time is very large because of the large size of the structures located in the corona.

2.6.6 Interplanetary Coronal Mass Ejections (ICME)

Farther in the corona and closer to the Earth and other planets, the CME develop into an ICME, where the magnetic field, contained in a magnetic cloud, plays such an important role when it impacts the magnetospheric field. When its sign is opposite to the sign of the terrestrial field, it leads to a large range of phenomena (radio bursts, precipitation of particles in the polar cusps, etc.) pertaining to the Space Weather. The ICME propagation is depicted in the cartoon of Fig. 2.32 from [33], which combines magnetic field, plasma, and solar wind suprathermal electron flows. The upstream shock contributes to accelerate particles. The shape of the plasma cloud
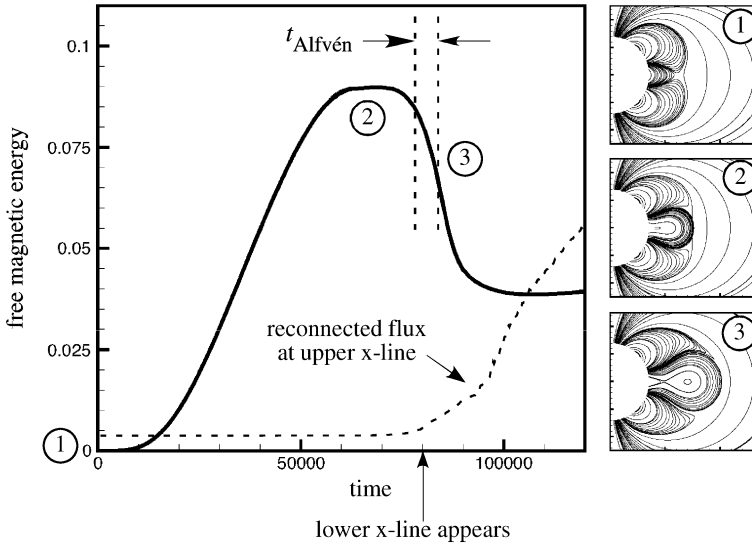
Fig. 2.31 Break out model. Right hand drawings display three different times of the eruption. In the quadrupolar magnetic structure (*top drawing 1*), the region between the two dipoles is prone to flux rise which takes place in the *middle drawing 2*. At the end of phase 2, an X-point appears, and magnetic reconnection takes place. Finally, the magnetic configuration (*lower drawing 3*) includes a plasmoid at the top, a current sheet below, and loops close to the surface. On the left-hand side, the free magnetic energy is plotted vs. time and the three different phases are shown: the free energy first strongly increases and then decreases when the reconnection takes place. Note that the Alfvén time is very large because of the large size of the structures located in the corona (from [37])

can be observed when it escapes in the plane of the sky of the instruments with the help of Heliospheric Imagers, as is the case for STEREO (Fig. 2.33). The quantity of material, and consequently the emission, is so faint that this requires very sensitive and clean instruments and a technique of image subtraction which allows one to visualize propagating plasmas. (It should be realized that the signal is smaller than that from a 12th magnitude star!)

2.7 The Heliosphere

It is an elongated bubble (Fig. 2.34) with a "radius" of about 100 AU, a distance which can be deduced from the equality of solar wind and interstellar medium pressures. It is bound by the interstellar medium of the Local cloud, "the low-pressure exit of the SW nozzle" according to [35]. Typical values there are: $n_H \sim 0.2$ cm^{-3}, $V = 26$ km s^{-1}, and $B = 2$–3 μG. With such figures, as shown by [35], the energy of the bulk plasma motion and the thermal and magnetic energies are about equal (a few 10^{-14} J m^{-3}). This energy density is of the order of the energy required
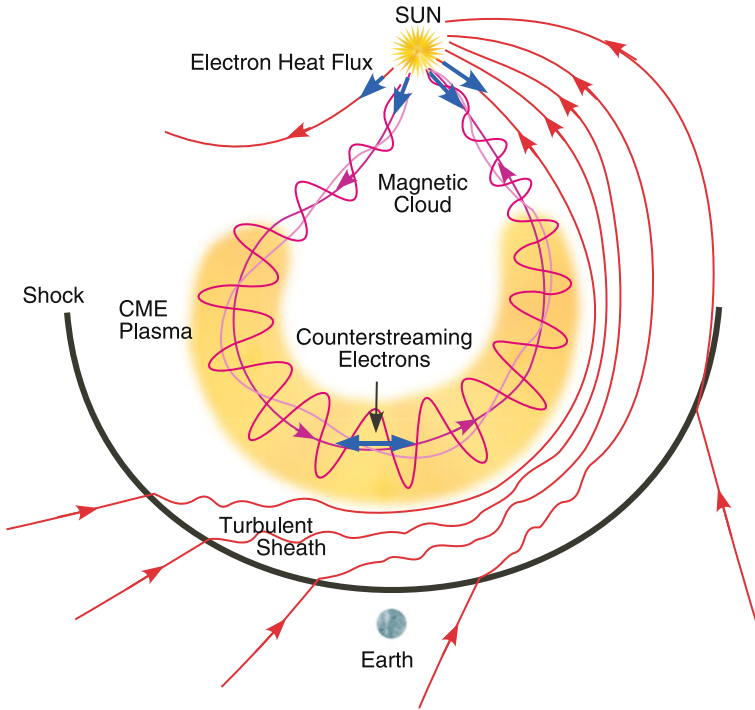
Fig. 2.32 Cartoon depicting magnetic field, plasma, and suprathermal flows in an ICME. Note the shock, already mentioned in Fig. 2.29 which also allows further particles acceleration (from [33])

by cosmic rays. Moreover, in this interface region, the importance of charge exchange between the fully ionized solar wind and the neutral interstellar medium is evidenced by "hydrogen walls," the generation of an important X-ray emission, the so-called anomalous cosmic rays. The interaction between heliosphere and interstellar medium is schematically depicted in Fig. 2.34, where one sees the backward return of the solar wind when it meets the interstellar medium at the level of a shock. What is fascinating is the fact that such bow shocks have been visualized close to their respective young stars in the Orion Nebula (Fig. 2.35). Their sizes are about 10^4 times the size of the heliosphere, and their mass flux is about 10^8 the mass flux in our heliosphere.

2.8 Conclusions and Prospects

As far as the solar wind is concerned, the need to fill the gap between measurements at a few solar radii and at 1 AU is evident since the remote-sensing spectroscopic measurements performed with UVCS/SOHO did not go higher than 5 solar radii on one hand, and the in situ measurements are mostly performed at 1 AU (apart
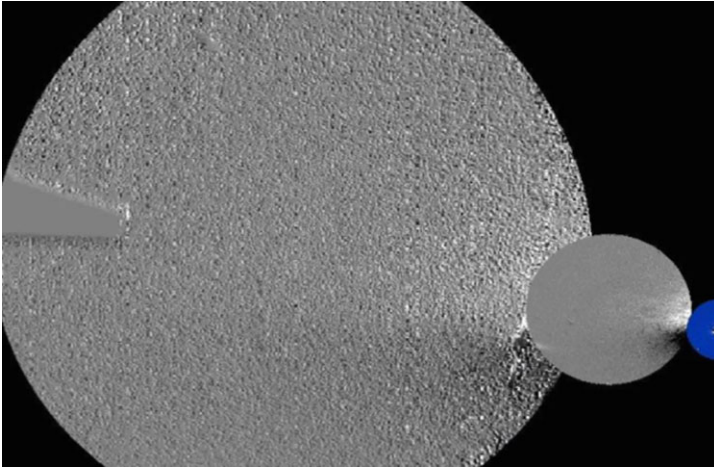
Fig. 2.33 This image is actually a movie obtained from the two Heliospheric Imagers on STEREO. On the right, the Sun is shown in EUV along with a coronagraph picture (in *blue*) from STEREO. The Earth is close to the left-hand side of the FOV of the most external heliospheric imager (the rocket-nose shaped black area corresponds to the Earth occulter). The movie catches the propagating CME with the technique of two-by-two images subtraction (courtesy STEREO Teams)
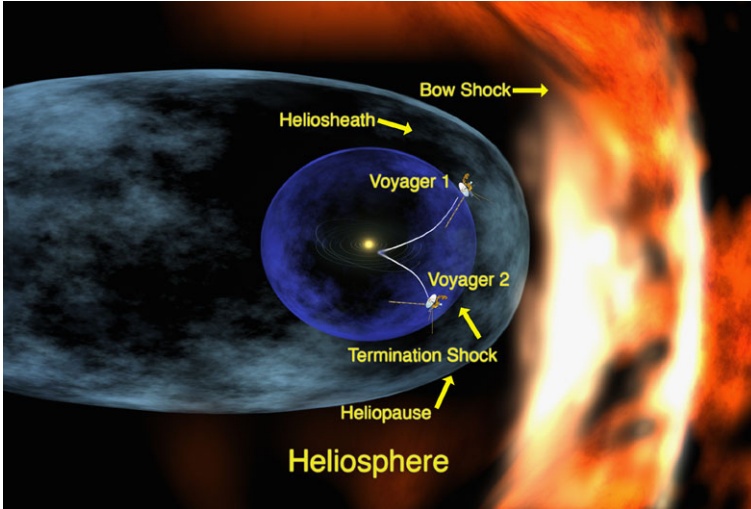

Fig. 2.34 Cartoon of the interface between the heliosphere and the interstellar medium. The Sun is drawn as a *yellow dot* with circling planet orbits. The *bright blue* sphere contains the interplanetary medium where the solar wind is supersonic. The termination shock marks the distance from where the solar wind becomes subsonic (heliosheath in *dark blue*). Further out, the heliopause marks the frontier with the interstellar medium. Note the bow shock ahead. Note the trajectories of Voyager 1 and 2 (courtesy Ed. Stone, from NASA/Walt Feimer)

Fig. 2.35 This is not a cartoon or an artist's rendering. These images of the Orion Nebula show, at the center and at the upper right, two bow shocks located very close to their respective young stars (courtesy Ed. Stone, from NASA/STScI/AURA)

Fig. 2.36 Electron density measurements performed in a current sheet (*top curve*) and in a coronal hole (*lower curve*). The measurements gap between 5 and 215 solar radii is well obvious (from [11])
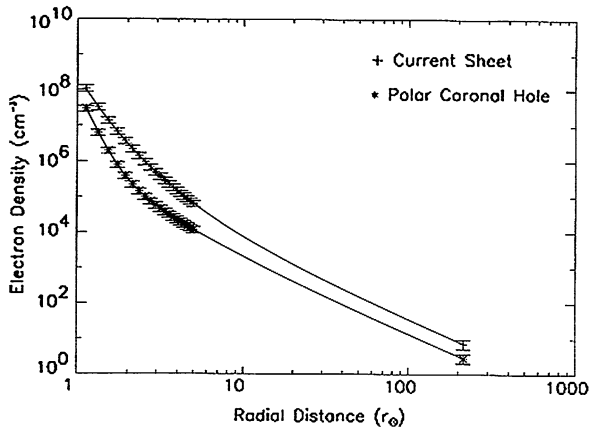
from the exceptional measurements of Helios which got closer than about 60 solar radii) on the other hand (Fig. 2.36). An answer to this gap consists in going closer to the Sun: the Solar Orbiter, approved on October 2011 by ESA, will sound the solar corona and the solar wind closer than 0.3 AU with a package of remote-sensing and in situ instruments far superior to SOHO instrumentation (Fig. 2.37). A peculiarity of the mission consists in reaching a 30 degrees latitudes allowing one to have a view on the polar coronal holes and the fast wind which originates from. The measurements will tackle the sources of the continuous and episodic flows of material (including energetic particles) and will record their transformations when they reach the S/C. The NASA Solar Probe$^+$ will go closer to the Sun (about 10 solar radii), and the set of in situ instruments will provide the "ground truth" for diagnosing the encountered plasma and magnetic field (Fig. 2.38). Scientists also dream of the combined information obtained with the two missions. Another major step consists to measure the coronal magnetic field in the lower corona (lower than the 10 solar
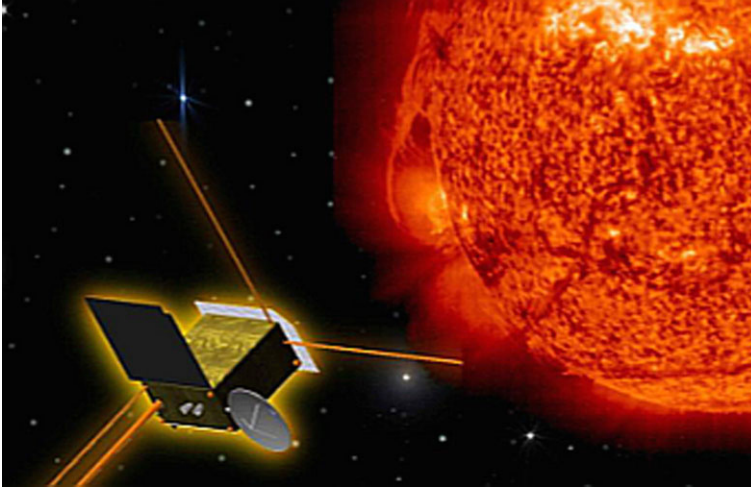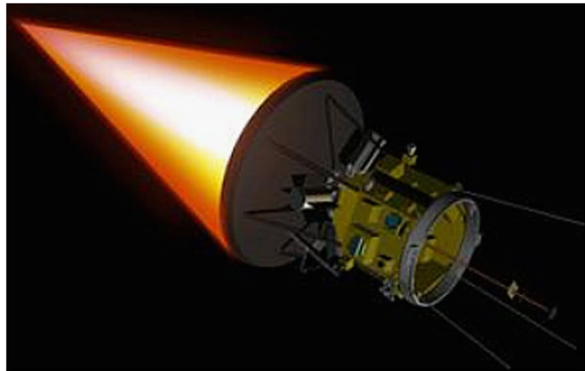
Fig. 2.37 Artist view of the ESA Solar Orbiter platform

Fig. 2.38 Artist view of the
NASA Solar Probe$^+$ platform

radii of Solar Probe$^+$): this is the aim of some Cosmic Vision proposals to ESA
(SOLMEX, LEMUR, etc.). Finally, the most challenging step is to understand bet-
ter the sources of the various events (including the wind) in the low corona, the
CCTR, and especially in the complex chromosphere. This will require better diag-
nostic tools and observations of the magnetic field, non-Maxwellian distributions,
ionization degrees, flows, etc., close to the (unknown) spatial scales where most
physical processes take place!

References

Main References

1. Amari, T., Luciani, J.F., Aly, J.J., Mikic, Z., Linker, J.: Coronal mass ejection: initiation, magnetic helicity, and flux ropes, II: turbulent diffusion-driven evolution. Astrophys. J. **595**, 1231–1250 (2003)
2. Antiochos, S.K., DeVore, C.R., Klimchuk, J.A.: A model for solar coronal mass ejections. Astrophys. J. **510**, 485–493 (1999)
3. Aschwanden, M.J., Poland, A.I., Rabin, D.M.: The new solar corona. Annu. Rev. Astron. Astrophys. **39**, 175 (2001)
4. Baker, D., van Driel-Gesztelyi, L., Mandrini, C.H., Démoulin, P., Murray, M.J.: Magnetic reconnection along quasi-separatrix layers as a driver of ubiquitous active region outflows. Astrophys. J. **705**, 926–935 (2009)
5. Banaszkiewicz, M., Axford, W.I., McKenzie, J.F.: An analytic solar magnetic field model. Astron. Astrophys. **337**, 940–944 (1998)
6. Biermann, L.: Solar corpuscular radiation and the interplanetary gas. Observatory **77**, 109 (1957)
7. Boutry, C., Buchlin, E., Vial, J.-C., Régnier, S.: Flows at the edge of an active region: observation and interpretation. Astrophys. J. **752**, 13 (2012)
8. David, C., Gabriel, A.H., Bely-Dubau, F., Fludra, A., Lemaire, P., Wilhelm, K.: Measurement of the electron temperature gradient in a solar coronal hole. Astron. Astrophys. **336**, L90 (1998)
9. De Pontieu, B., McIntosh, S.W., Carlsson, M., Hansteen, V.H., Tarbell, T.D., Boerner, P., Martinez-Sykora, J., Schrijver, C.J., Title, A.M.: The origins of hot plasma in the solar corona. Science **331**, 55 (2011)
10. Gabriel, A., Bely-Dubau, F., Tison, E., Wilhelm, K.: The structure and origin of solar plumes: network plumes. Astrophys. J. **700**, 551–558 (2009)
11. Guhathakurta, M., Sittler, E.: Importance of global magnetic field geometry and density distribution in solar wind modeling. In: Habbal, S.R., Esser, R., Hollweg, J.V., Isenberg, P.A. (eds.) American Institute of Physics Conference Series, vol. 471, pp. 79–82 (1999)
12. Harra, L.K., Sakao, T., Mandrini, C.H., Hara, H., Imada, S., Young, P.R., van Driel-Gesztelyi, L., Baker, D.: Outflows at the edges of active regions: contribution to solar wind formation? Astrophys. J. Lett. **676**, L147–L150 (2008)
13. Hassler, D.M., Dammasch, I.E., Lemaire, P., Brekke, P., Curdt, W., Mason, H.E., Vial, J.-C., Wilhelm, K.: Solar wind outflow and the chromospheric magnetic network. Science **283**, 810 (1999)
14. He, J.-S., Marsch, E., Tu, C.-Y., Guo, L.-J., Tian, H.: Intermittent outflows at the edge of an active region—a possible source of the solar wind? Astron. Astrophys. **516**, A14 (2010)
15. Kahler, S.W.: Solar sources of heliospheric energetic electron events: shocks or flares? Space Sci. Rev. **129**, 359 (2007)
16. Kohl, J.L., Noci, G., Antonucci, E., Tondello, G., Huber, M.C.E., Cranmer, S.R., Strachan, L., Panasyuk, A.V., Gardner, L.D., Romoli, M., Fineschi, S., Dobrzycka, D., Raymond, J.C., Nicolosi, P., Siegmund, O.H.W., Spadaro, D., Benna, C., Ciaravella, A., Giordano, S., Habbal, S.R., Karovska, M., Li, X., Martin, R., Michels, J.G., Modigliani, A., Naletto, G., O'Neal, R.H., Pernechele, C., Poletto, G., Smith, P.L., Suleiman, R.M.: UVCS/SOHO empirical determinations of anisotropic velocity distributions in the solar corona. Astrophys. J. Lett. **501**, L127 (1998)
17. Le Chat, G., Issautier, K., Meyer-Vernet, N., Hoang, S.: Large-scale variation of solar wind electron properties from quasi-thermal noise spectroscopy: Ulysses measurements. Sol. Phys. **271**, 141 (2011)

18. Marsch, E., Schwenn, R., Rosenbauer, H., Muehlhaeuser, K.-H., Pilipp, W., Neubauer, F.M.: Solar wind protons—three-dimensional velocity distributions and derived plasma parameters measured between 0.3 and 1 AU. J. Geophys. Res. **87**, 52–72 (1982)
19. Masuda, S., Kosugi, T., Hara, H., Tsuneta, S., Ogawara, Y.: A loop-top hard X-ray source in a compact solar flare as evidence for magnetic reconnection. Nature **371**, 495–497 (1994)
20. McComas, D.J., Bame, S.J., Barraclough, B.L., Feldman, W.C., Funsten, H.O., Gosling, J.T., Riley, P., Skoug, R., Balogh, A., Forsyth, R., Goldstein, B.E., Neugebauer, M.: Ulysses' return to the slow solar wind. Geophys. Res. L ett. **25**, 1–4 (1998)
21. Murphy, R.J., Share, G.H.: What gamma-ray deexcitation lines reveal about solarflares. Adv. Space Res. **35**, 1825–1832 (2005)
22. Noci, G.: Diagnostic methods for the extended corona. Adv. Space Res. **11**, 263 (1991)
23. Parker, E.N.: Dynamics of the interplanetary gas and magnetic fields. Astrophys. J. **128**, 664 (1958)
24. Patsourakos, S., Vial, J.-C.: Outflow velocity of interplume regions at the base of polar coronal holes. Astron. Astrophys. **359**, L1–L4 (2000)
25. Sakao, T., Kano, R., Narukage, N., Kotoku, J., Bando, T., DeLuca, E.E., Lundquist, L.L., Tsuneta, S., Harra, L.K., Katsukawa, Y., Kubo, M., Hara, H., Matsuzaki, K., Shimojo, M., Bookbinder, J.A., Golub, L., Korreck, K.E., Su, Y., Shibasaki, K., Shimizu, T., Nakatani, I.: Continuous plasma outflows from the edge of a solar active region as a possible source of solar wind. Science **318**, 1585 (2007)
26. Schwenn, R., Inhester, B., Plunkett, S.P., Epple, A., Podlipnik, B., Bedford, D.K., Eyles, C.J., Simnett, G.M., Tappin, S.J., Bout, M.V., Lamy, P.L., Llebaria, A., Brueckner, G.E., Dere, K.P., Howard, R.A., Koomen, M.J., Korendyke, C.M., Michels, D.J., Moses, J.D., Moulton, N.E., Paswaters, S.E., Socker, D.G., St. Cyr, O.C., Wang, D.: First view of the extended green-line emission corona at solar activity minimum using the Lasco-C1 coronagraph on SOHO. Sol. Phys. **175**, 667–684 (1997)
27. Sheeley, N.R. Jr., Wang, Y.-M., Hawley, S.H., Brueckner, G.E., Dere, K.P., Howard, R.A., Koomen, M.J., Korendyke, C.M., Michels, D.J., Paswaters, S.E., Socker, D.G., St. Cyr, O.C., Wang, D., Lamy, P.L., Llebaria, A., Schwenn, R., Simnett, G.M., Plunkett, S., Biesecker, D.A.: Measurements of flow speeds in the corona between 2 and 30 R sub sun. Astrophys. J. **484**, 472 (1997)
28. Tu, C.-Y., Zhou, C., Marsch, E., Xia, L.-D., Zhao, L., Wang, J.-X., Wilhelm, K.: Solar wind origin in coronal funnels. Science **308**, 519–523 (2005)
29. Vial, J.-C., Auchère, F., Chang, J., Fang, C., Gan, W.Q., Klein, K.-L., Prado, J.-Y., Rouesnel, F., Sémery, A., Trottet, G., Wang, C.: SMESE (SMall Explorer for Solar Eruptions): a microsatellite mission with combined solar payload. Adv. Space Res. **41**, 183–189 (2008)
30. Wang, Y.-M., Sheeley, N.R. Jr., Walters, J.H., Brueckner, G.E., Howard, R.A., Michels, D.J., Lamy, P.L., Schwenn, R., Simnett, G.M.: Origin of streamer material in the outer corona. Astrophys. J. Lett. **498**, L165 (1998)
31. Wilhelm, K., Dammasch, I.E., Marsch, E., Hassler, D.M.: On the source regions of the fast solar wind in polar coronal holes. Astron. Astrophys. **353**, 749–756 (2000)
32. Wilhelm, K., Abbo, L., Auchère, F., Barbey, N., Feng, L., Gabriel, A.H., Giordano, S., Imada, S., Llebaria, A., Matthaeus, W.H., Poletto, G., Raouafi, N.-E., Suess, S.T., Teriaca, L., Wang, Y.-M.: Morphology, dynamics and plasma parameters of plumes and inter-plume regions in solar coronal holes. Astron. Astrophys. Rev. **19**, 35 (2010)
33. Zurbuchen, T.H., Richardson, I.G.: In-situ solar wind and magnetic field signatures of interplanetary coronal mass ejections. Space Sci. Rev. **123**, 31–43 (2006)

General References About Solar Wind

34. Marsch, E.: In: Space Solar Physics. Lecture Notes in Physics, vol. 507, p. 107 (1998)
35. Meyer-Vernet, N.: Basics of the Solar Wind. Cambridge University Press, Cambridge (2007)
36. Velli, M.: In: Space Solar Physics. Lecture Notes in Physics, vol. 507, p. 217 (1998)

General References About Flares, CMEs, Erupting Prominences

37. Forbes, T., et al.: CME theory and models. Space Sci. Rev. **123**, 251–302 (2006)
38. Schrijver, C.J.: Driving major solar flares and eruptions: a review. Adv. Space Res. **43**(5), 739–755 (2009)

General References About Prominences

39. Labrosse, N., Heinzel, P., Vial, J.-C., et al.: Space Sci. Rev. **151**, 243 (2010)
40. MacKay, M., Karpen, J., Ballester, J.L., et al.: Space Sci. Rev. **151**, 1 (2010)
41. Schrijver, C.J.: Solar energetic events, the solar-stellar connection, and statistics of extreme space weather. In: Proceedings of the 16th Workshop on Cool Stars, Stellar Systems, and the Sun. PASP Conference Series (2010)